Destabilization of the human RED–SMU1 splicing complex as a basis for host-directed antiinfluenza strategy

Usama Ashraf, Laura Tengo, Laurent Le Corre, Guillaume Fournier, Patricia Busca, Andrew Mccarthy, Marie-Anne Rameix-Welti, Christine Gravier-Pelletier, Rob W H Ruigrok, Yves Jacob, et al.

Destabilisation of the human RED-SMU1 splicing complex as a basis for host-directed anti-influenza therapy

Usama Ashraf[1,2,3], Laura Tengo[4], Laurent Le Corre[5], Guillaume Fournier[1,2,3], Patricia Busca[5], Andrew A. McCarthy[6], Marie-Anne Rameix-Welti[7,8], Christine Gravier-Pelletier[5], Rob W.H. Ruigrok[4], Yves Jacob[1,2,3], Pierre-Olivier Vidalain[9], Nicolas Pietrancosta[9*],Thibaut Crépin[4*], Nadia Naffakh[1,2,3*]

[1] Institut Pasteur, Unité de Génétique Moléculaire des Virus à ARN, Département de Virologie, Paris, France
[2] CNRS, UMR3569, Paris, France
[3] Université Paris Diderot, Sorbonne Paris Cité, EA302, Paris, France
[4] Institut de Biologie Structurale (IBS), Université Grenoble Alpes, CEA, CNRS, Grenoble, France
[5] Université Paris Descartes, CNRS UMR 8601, Laboratoire de Chimie et Biochimie Pharmacologiques et Toxicologiques, Equipe Synthèse Organique pour la Recherche Biomédicale, Paris, France.
[6] EMBL Grenoble, 71 avenue des Martyrs, CS 90181, Grenoble, France
[7] UMR1173, INSERM, Université de Versailles St. Quentin, Montigny le Bretonneux, France
[8] AP-HP, Laboratoire de Microbiologie, Hôpital Ambroise Paré, Boulogne-Billancourt, France
[9] Université Paris Descartes, CNRS UMR 8601, Laboratoire de Chimie et Biochimie Pharmacologiques et Toxicologiques, Equipe Chimie & Biologie, Modélisation et Immunologie pour la Thérapie, Paris, France.

* correspondence :
nadia.naffakh@pasteur.fr (N. Naffakh)
Thibaut.Crepin@ibs.fr (T. Crépin)
nicolas.pietrancosta@parisdescartes.Fr (N. Pietrancosta)

Classification :

Major : Biological Sciences

Minor : Microbiology

Abstract

New therapeutic strategies targeting influenza are actively sought due to limitations in current drugs available. Host-directed therapy is an emerging concept to target host functions involved in pathogen life cycles and/or pathogenesis, rather than pathogen components themselves. From this perspective, we focused on an essential host partner of influenza viruses, the RED-SMU1 splicing complex. Here we identified two synthetic molecules targeting an α-helix-groove interface essential for RED-SMU1 assembly. We solved the structure of SMU1 N-terminal domain in complex with RED or bound to one of the molecules identified to disrupt this complex. We show that these compounds inhibiting RED-SMU1 interaction also decrease endogenous RED-SMU1 levels, inhibit viral mRNA splicing and viral multiplication, whilst preserving cell viability. Overall, our data demonstrate the potential of RED-SMU1 destabilizing molecules as a novel antiviral therapy, which could be active against a wide range of influenza viruses and be less prone to drug resistance.

Keywords : Influenza virus, Splicing, Structure-based drug screening, Host-directed antivirals

Significance Statement

Influenza virus is a serious threat to global public health and there is a critical need for innovative anti-influenza drugs. Two broad, non-exclusive approaches to inhibit viral replication are possible, either targeting directly viral proteins or targeting host proteins essential for the viral life cycle. Here we took the second approach, which is more likely to counter the problem of drug-resistant virus emergence. Focusing on an essential host partner of influenza viruses, the RED-SMU1 splicing complex, we performed a virtual structure-based drug screening. We identified two synthetic molecules which interfere with RED-SMU1 complex assembly, inhibit the splicing of viral messenger RNAs, and show potential for the inhibition of influenza virus infections.

\body

Introduction

The increasing incidence of drug-resistant pathogens calls for the development of novel therapeutic strategies. In recent years, the concept of host-directed therapies, which target host determinants essential for the infectious life cycle and/or pathogenesis rather than pathogens components, has been rapidly expanding (1, 2). Preclinical studies suggest they could show clinical safety while providing the advantage of broad spectrum efficacy and reduced antiviral resistance. A range of host-directed therapies for several bacterial and viral diseases, with different mechanisms of action, are currently in clinical trials (1, 2).

Influenza A viruses (IAVs) are a leading cause of morbidity and mortality worldwide, as they are responsible for recurring annual epidemics, frequent epizootics, and occasional pandemics (3). The drugs currently licensed for treatment of influenza target viral components (the M2 ion channel, the neuraminidase and the polymerase) and they all lead to the emergence of resistance variants. The M2 inhibitors are no longer recommended for use since currently circulating human H3N2 and H1N1pdm09 viruses have become naturally resistant to these drugs (4). Although the frequency of resistance to neuraminidase inhibitors (NAIs) of currently circulating human IAVs remains low (around 0.5%) (5), large clusters of H1N1pmd09 viruses resistant to oseltamivir, the most widely used NAI, have been observed (6, 7). The former seasonal H1N1 IAVs had become globally oseltamivir-resistant during the 2007-2008 season (8). Favipiravir, a purine nucleoside analog also known as T-705, is undergoing phase III trials in America and Europe and has been approved in Japan to treat pandemic influenza virus infections. In October 2018, FDA approved Xofluza, a selective inhibitor of the polymerase PA subunit, for the treatment of acute uncomplicated influenza. However, the first evidence for viral adaptation to favipiravir treatment in cell culture has been reported recently (9, 10), and the emergence of PA variants with a mutation conferring resistance to Xofluza was observed in 9.7% of treated patients in the Phase III trial (11). In this context, novel anti-influenza drugs are actively being sought to efficiently fight IAVs, particularly with regard to pandemic preparedness (12, 13). Antivirals currently in late-phase clinical trials include monoclonal antibodies against the viral hemagglutinin or matrix protein

(14, 15), a selective inhibitor of the polymerase PB2 subunit (16), and two compounds targeting host cell factors: nitaxozanide, which impairs trafficking and maturation of the viral hemagglutinin (HA) (17, 18); and DAS181, which enzymatically removes the membrane receptors required for IAV attachment to target cells (19, 20). Continuous progress on the identification of host factors involved in IAV life cycle provides a basis for the development of alternative host-directed antiviral drugs (21, 22). Following this approach we have characterized the structure of a human splicing factor, RED-SMU1, that is essential for IAV life cycle, and exploited the structural data to investigate this cellular factor as a potential target for IAV therapy.

Infectious IAV particles contain eight ribonucleoprotein complexes (vRNPs), corresponding to a set of eight distinct viral genomic RNA (vRNA) segments encapsidated with nucleoproteins (NP) and associated with the heterotrimeric viral RNA-dependent RNA polymerase (FluPol) consisting of the PB1, PB2 and PA subunits (3). The viral genome has a limited size (about 13.5 kb), but IAVs have evolved a variety of strategies to expand their coding capacity. Viral mRNAs are synthesized by the FluPol in the nucleus of infected cells. Although most of these are intronless, the M, NS and PB2 segments produce both unspliced mRNAs (M1, NS1, PB2) and spliced mRNAs (M2, NS2, PB2-S1). We previously showed that FluPol recruits a complex formed by the human splicing factors RED (78.9 kDa) and SMU1 (57.5 kDa) by direct binding to RED (23). RED-SMU1 regulates the splicing of viral NS1 mRNA into the mRNA encoding the multifunctional and essential NS2/NEP protein. In cells depleted for RED or SMU1, the production of infectious influenza virions showed a 100-fold reduction (23), designating the RED-SMU1 complex as a promising IAV drug target.

The RED and SMU1 factors are associated to the pre-catalytic spliceosome (24). They were found to jointly regulate the splicing of specific cellular pre-mRNAs, with a possible role in the selection of cryptic 5' splice sites (25-27). As we and others have observed that RED and SMU1 directly bind (23, 26, 28) and stabilize each other (23, 26, 27), a significant proportion of functional RED-SMU1 complexes is likely to exist.

Here we performed subdomain analysis of human RED and SMU1 proteins using cell-based interaction assays, and solved the crystal structure of a minimal RED-SMU1 complex at 3.0 Å resolution. The structure shows similarities to the recently published RED and SMU1 orthologs in *Caenorhabditis elegans* (*ce*RED and *ce*SMU1) (29) but reveals a more intricate RED-SMU1 interface. Based on our structural findings, we identified small molecules that target an α-helix-groove interface essential for RED-SMU1 interaction. Lastly, we provide supporting data to demonstrate the potential of such RED-SMU1 destabilizing molecules for the inhibition of IAV infections.

Results

Delineation of a minimal RED-SMU1 complex

We previously found that the N-terminal domain of RED (residues 1 to 315) binds to SMU1 as efficiently as the full-length RED protein (23). Using a split-luciferase based interaction assay, we further delineated a minimal human RED-SMU1 complex. Plasmids encoding various subdomains of RED tagged with the Gluc2 fragment of *Gaussia princeps* luciferase were co-transfected with plasmids for the expression of SMU1 or $SMU1_{Nter}$ (residues 1-196) fused to the trans-complementing *Gaussia princeps* luciferase Gluc1 fragment. The rationale for RED truncations shown in **Fig. 1A** was based on secondary structure and disorder predictions (**SI Appendix, Fig. S1**), with an iterative testing and design approach. As revealed by the relative luciferase activities measured in cell extracts, the RED[206-260] subdomain (named thereafter RED_{mid}) retained the interaction with SMU1 (black bars) or $SMU1_{Nter}$ (grey bars) (**Fig. 1A**). The SMU1 interaction signals were almost 8-fold higher with RED_{mid} than with the full-length RED ($p<0.01$), and were higher than with any longer truncated version of RED. Western blot analysis of the cell lysates used for luciferase assay showed that this higher interaction signal was not due to a higher level of expression of RED_{mid} (**Fig. 1B**, black arrowhead) compared to other deletion mutants of RED or to the full-length RED (open arrowhead). A likely explanation is that the short RED_{mid} subdomain is more stable thermodynamically than the longer versions of RED and that it becomes more accessible upon removal of the adjacent polypeptides. For several other protein pairs, it was indeed previously shown that interactions are more easily detected when using isolated interacting subdomains or peptides (30). Notably, the RED[219-299] subdomain produced lower interaction signals compared to RED_{mid} but also to the full-length RED protein, suggesting that residues 206 to 218 of RED are essential for the interaction with SMU1.

The 3D structure of human RED_{mid}-$SMU1_{Nter}$ reveals two molecular interfaces

Based on our cell-based interaction results, we set up a co-expression strategy to produce and pull-down the human RED_{mid}-$SMU1_{Nter}$ complex, using a hexa-histidine tag fused to the N-terminus of RED_{mid}. The recombinant complex was crystallized and the structure solved by molecular replacement using the X-ray structure of the $SMU1_{Nter}$ alone without RED_{mid} obtained earlier (**SI Appendix, Fig. S2 and Table S1**). The final model was built using the anomalous signal of a Se-met derivative dataset for an accurate sequence assignment. The asymmetric unit is composed of sixteen molecules: eight $SMU1_{Nter}$ molecules that assemble into four dimers, and eight RED_{mid} molecules each one being associated with a $SMU1_{Nter}$ monomer. The X-ray structure reveals two distinct interfaces between $SMU1_{Nter}$ and RED_{mid} (**Fig. 2A**). First, the region of RED_{mid} corresponding to residues 235-257 disrupts the initial fold of the N-terminus of $SMU1_{Nter}$ to form a three-stranded antiparallel β-sheet, that is uniquely stabilized by main chain interactions (Interface I, **Fig. 2B)**. Second, the helical region of RED_{mid} (corresponding to residues 211-221) lies in a hydrophobic groove delimited by three continuous α-helices (α4 to α6) on the surface of $SMU1_{Nter}$ (Interface II, **Fig. 2C)**. The structural results are consistent with the high and low interaction signals measured with the SMU1-RED[206-260] and SMU1-RED[219-299] combinations, respectively (**Fig. 1A**).

The comparison of our human RED_{mid}-$SMU1_{Nter}$ structure with the recently published structure of a *C. elegans* minimal RED-SMU1 complex ((29) and **SI Appendix, Fig. S3**) is discussed below. Importantly, the human structure suggests that SMU1 needs to form a dimer to assemble with RED, as Interface I extends across two distinct $SMU1_{Nter}$ monomers. In agreement with this observation, SEC-MALLS analysis on purified full-length SMU1 protein showed that it is mostly dimeric (**Fig. S4A**), and treatment of A549 or HEK-293T cells with the cell-permeable crosslinking agent disuccinimidyl suberate (DSS) followed by western blotting revealed that the endogenous SMU1 protein forms dimers in live cells (**Fig. S4B**).

Mutational analysis provides a rationale for targeting the α-helix:groove interface

To confirm our structural data and assess the druggability of the RED-SMU1 interface, we performed structure-based mutational analysis of the full-length RED and SMU1 proteins. Point mutations were introduced at interface I (**Fig. 2B**) or II (**Fig. 2C** and **Fig. 3A-B**). Split-luciferase complementation assays were performed and expression levels of the mutants were assessed (**Fig. 3C-H**). Short deletions in the domains of SMU1 (Δ3-7) or RED (Δ237-241 or Δ254-256) involved in interface I reduced the RED-SMU1 interaction signal up to 3-fold (**Fig. 3C**, black bars). In the presence of SMU1 mutations targeting the interface II (D57A-E89A, L60D-I63D, L73D-Y77D, L84D-L87D) or the hinge between interface I and II (P157T-P158T), a 2- to 10-fold reduction of the interaction signal was also observed (**Fig. 3D**). Notably, no cumulative effect was observed when deletions at interface I were combined with the SMU1 mutations D57A-E89A destabilizing interface II (**Fig. 3C**, grey bars), suggesting that both molecular interfaces are required to stabilize the RED-SMU1 complex. RED mutants L212D, V216D and L220D targeting interface II showed a 2-fold reduction of the interaction signals with SMU1 or SMU1-D57Q (**Fig. 3E**). In contrast the RED-N215D and M219D mutations had little effect on the interaction with SMU1 (**Fig. 3E**), as expected from the 3D structure (**Fig. 3A-B**). Together, these results confirm our structural findings, demonstrate that a mere disruption of interface II α-helix:groove impairs the stability of the RED-SMU1 complex, and point to SMU1 D57, L60, I63, L73, Y77, L84, L87 and E89 as key RED binding residues.

Disrupting the RED-SMU1 complex: proof-of-principle by overexpressing RED$_{mid}$

Based on the data presented above, we reasonned that if overexpressed, the RED$_{mid}$ helical domain should efficiently compete with the full-length RED protein for binding to the surface groove on SMU1, and thereby disrupt the RED-SMU1 complex. As a control, we used a RED$_{mid}$-V216D mutant, which accumulates at the same levels as RED$_{mid}$ but is strongly impaired for SMU1 binding. Of note, the effect of V216D mutation on SMU1 binding is much stronger in the context of RED$_{mid}$ (> 99% reduction) compared to the full-length RED (about

50% reduction) (**SI Appendix, Fig. S5A**). Upon overexpression of the mCherry-RED_{mid} fusion protein we observed a >2-fold reduction of the RED-SMU1 interaction signal, as measured with the split-luciferase complementation assay, while with the control mCherry-RED_{mid}-V216D mutant, no such reduction was observed ($p<0.01$, **SI Appendix, Fig. S5B-C**). We then assessed the effect of RED_{mid} overexpression on the endogenous RED-SMU1 complex. As there is evidence that RED and SMU1 stabilize each other (23, 26, 27), RED-SMU1 disruption is expected to result in decreased steady-state levels of the proteins. We observed a decrease in endogenous cellular levels of RED when overexpressing RED_{mid}, whereas empty vectors or RED_{mid}-V216D had no effect (**Fig. S5D**, upper panel). However, SMU1 levels remained unchanged (**Fig. S5D**, middle panel). A likely interpretation is that the SMU1 protein complexed with RED_{mid} remains stable, whereas the dissociated RED protein undergoes degradation.

Next we monitored the effect of RED_{mid} overexpression on the replication of a recombinant A/WSN/33 virus carrying a luciferase reporter gene (WSN-PB2-Nanoluc). The luciferase activity measured in cell lysates prepared at 24 hours post-infection (hpi), was lower in cells overexpressing RED_{mid} compared to cells transfected with the empty pCI vector or overexpressing RED_{mid}-V216D (**Fig. S5E**). On the contrary, there was no significant difference between cells transfected with the empty pCI vector and those overexpressing RED_{mid}-V216D. Furthermore, splicing of the viral NS1 mRNA into NS2 mRNA, which is dependent upon RED-SMU1 (23), was reduced in RED_{mid}-expressing cells compared to the RED_{mid}-V216D control (**Fig. S5F**). Overall, our findings strengthen the rationale of targeting the RED-SMU1 α-helix:groove interface to inhibit IAV replication.

In silico identification and evaluation of RED-SMU1 disrupting compounds

We used the available structural information on the RED_{mid}-$SMU1_{Nter}$ complex to perform molecular docking-based screening for compounds targeting the RED-binding groove at the surface of $SMU1_{Nter}$. The virtual high-throughput screening (vHTS) was performed on a set of 4,121 chemical compounds from our in-house chemical database (LCPBT-DB), comparable

to the Prestwick or FDA-approved libraries in terms of chemical diversity (see **SI Appendix**). A flow chart for the vHTS and compound selection pipeline is represented in **Fig. 4A**. To ensure a time/precision ratio compatible with vHTS we used a protocol in which amino acid side chains of the protein are left flexible only around the binding site, and we tested 10 random conformers for each ligands. The resulting poses were ranked according to their docking scores, as described in the Methods section. The poses with the highest docking scores were further filtered to select for compounds that are predicted to bind at least 4 of the 8 SMU1 residues required for efficient binding to RED: D57, L60, I63, L73, Y77, L84, L87, E89 (**Fig. 4B** and **Fig. 3D**). A total of 37 compounds fulfilled both criteria, and a subset of 16 molecules with representative chemical scaffolds were further evaluated.

Among these, 14 showed no or only limited cytotoxicity at 60 µM, and were further tested at the same concentration in cell-based assays for the inhibition of RED-SMU1 interaction and IAV replication. Compounds inhibiting RED-SMU1 interaction by more than 20%, and IAV replication by more than 80% were selected for further evaluation. In total, three compounds showed promising inhibitory effect in both assays (**Fig. 4A**). Of these, one molecule, LSP641 (**Fig. 4C)**, was successfully co-crystallised with the purified recombinant $SMU1_{Nter}$ domain. Structural data showed that LSP641 locates in the hydrophobic RED binding pocket of SMU1 as expected (**Fig. 4D**) and is engaged in several molecular interactions with SMU1 (**Fig. 4E**). The 2-amino-pyrimidine group present in LSP641 forms key hydrogen bounds with Q61 and Q64, whereas the urea group forms a hydrogen bond with Y77. In the apolar region of SMU1, D57, L60 and L96 are involved in Pi-Pi or σ-Pi interactions, in particular with the pyridopyrimidine scaffold of LSP641. Furthermore, W56, I63, L84 and A92 form hydrophobic interactions with LSP641. Remarkably, the LSP641 molecule interacts with D57, L60, I63, Y77 and L84, *i.e*. 5 of the 8 residues shown earlier to be involved in RED-SMU1 interaction, to account for the inhibition of this protein-protein interaction.

Guided by the $SMU1_{Nter}$:LSP641 co-structure, we selected 27 LSP641-related compounds and we filtered them through a second evaluation round (**Fig. 4A**), which led to the selection of LSP61 (31) (**Fig. 4C and 4F**). Unfortunately, we were unable to co-crystallize LSP61 with

SMU1 $_{Nter}$. This different behavior of LSP61 compared to LSP641 might be related to the absence/presence of stacking interactions in the co-crystal. However, *in silico* molecular docking supported binding interactions similar to LSP641 (**Fig. 4G**). Hydrogen bonds with Q64 and Y77 are conserved, as well as Pi- or σ-Pi-interactions with D57 and L60, and hydrophobic interactions with W56 and L84. Q61 is involved in Pi-interactions, whereas V41, V80 and L96 are forming novel hydrophobic interactions. Most importantly, the benzylpiperidine group of LSP641 that is not binding SMU1 in the crystal structure (**Fig. 4D-E)**, is replaced in LSP61 by an alkyl chain which interacts with A62 and V41 in a neighboring hydrophobic pocket of SMU1 and therefore optimizes molecular recognition (**Fig. 4F-G**). This led us to select LSP61 to conduct further investigations, in parallel with LSP641.

LSP61 and LSP641 were compared in the RED-SMU1 interaction assay across the 0.23 to 60 µM concentration range. The EC50 (half-maximal effective concentration) was estimated to be 15 µM for LSP61 ; LSP641 showed a milder effect resulting in a 40% inhibition at 60 µM, compared to 90% with LSP61, and a plateauing curve (**Fig. 5A**). When a similar FOS:JUN interaction assay was used as a specificity control, none of the two compounds showed any significant effect (**Fig. 5B**). The Kd of the SMU1$_{Nter}$-LSP61 complex could not be determined, most likely due to the low solubility of LSP61 (logP=4.8). The effect of LSP61 on the endogenous RED-SMU1 complex was assessed using the steady-state levels of RED and SMU1 as a proxy. Expression levels of both proteins decreased when treating cells with 15, 30 and 60 µM LSP61 (**Fig. 5C**). At these concentrations, no cytotoxicity but some cytostatic effect was observed as assessed by the steady levels of ATP measured in culture wells (a proxy for cell count) upon 24 and 48 hours of incubation with LSP61 (**Fig. 5D)** and the observation of cell monolayers by bright field miscroscopy (**SI Appendix, Fig. S6**).

LSP61 inhibits IAV replication

Finally we assessed the ability of LSP61 to inhibit IAV replication. We first used the WSN-PB2-Nanoluc virus, in parallel with a recombinant human Respiratory Syncytial Virus (RSV) expressing Firefly luciferase as a specificity control (RSV replicates in the cytoplasm with no

direct involvement of the nuclear splicing machinery postulated). After viral adsorption to A549 cells, the LSP61 or LSP641 compounds were added to the cells across the 7.5 - 60 µM concentration range, and the luciferase activities were determined at 24 hpi. The RSV-Firefly signals showed only moderate reductions (**Fig. 6A**, grey bars). In contrast the WSN-Nanoluc signals showed a significant, dose-dependent reduction, more pronounced for LSP61 (25-fold at 60 µM, $p<0.0001$) compared to LSP641 (6-fold at 60 µM, $p<0.005$) (**Fig. 6A**, black bars). Growth kinetics were performed with wild-type IAVs (the WSN virus and representatives of H1N1pdm09 and H3N2 circulating human IAVs) in the presence of 60 µM LSP61 and the supernatants were titrated by plaque assay. Because the H1N1pdm09 and H3N2 isolates grew poorly on A549 cells, canine MDCK-SIAT cells (32) were used in these experiments. In the presence of LSP61 the production of infectious particles showed a 10- to 100-fold reduction at 24 and 48 hpi (**Fig. 6B**). In comparison, on A549 cells, the production of WSN infectious particles was reduced about 1000-, 100- and 10-fold at 24, 48 and 72 hpi, respectively (**Fig. 6C**). In MDCK-SIAT cells, canine Mx proteins lack anti-influenza activity, which limits the establishment of a strong interferon-induced antiviral state and favors a very efficient replication of influenza viruses (33). This particular feature of MDCK-SIAT cells likely accounts for the fact that a strong inhibition with the LSP61 compound was more difficult to achieve compared to in A549 cells.

In WSN-infected cells, the LSP641 and LSP61 compounds inhibited the splicing of the viral NS1 mRNA into NS2 mRNA at 60 µM concentration. Indeed, the NS2 to NS1 mRNA ratio was reduced by 30% with LSP641, and 50% with LSP61 (**Fig. 6D**), which is comparable to previous results obtained when either RED or SMU1 was knocked-down in infected cells (23). In contrast LSP641 and LSP61 did not inhibit the splicing of the viral M1 mRNAs (**Fig. S7A**), in agreement with our previous findings that M1 mRNA splicing is little affected by RED or SMU1 silencing compared to NS1 mRNA splicing (23). Likewise, PB2 mRNA splicing, whose role in viral infection remains unclear (34), is not affected by 60 µM LSP641 or LSP61 (**Fig. S7B**). The specificity of LSP641 and LSP61 towards the splicing of NS1 mRNA, taken together with our findings that both compounds inhibit RED-SMU1 interaction

(**Fig. 5A**) and IAV replication (**Fig. 6A**), with the observed effects being consistently more pronounced for LSP61, strongly argue for their antiviral effect being due to disruption of the RED-SMU1 complex.

Discussion

We have determined the crystal structure of the interacting human SMU1 N-terminal region ($SMU1_{Nter}$) and RED central region (RED_{mid}). As expected from the high conservation of these two protein subdomains, the observed structure shows similarity to the one reported for *C. elegans* (29). In both structures $SMU1_{Nter}$ assembles into a dimer through inter-molecular contacts between LisH motifs (**SI Appendix, Fig. S2**). Interestingly our structure reveals a more intricate SMU1-RED interaction with two binding interfaces, including a ß-sheet:ß-sheet interface (not present in the *C. elegans* structure) in addition to an α-helix:groove (**SI Appendix, Fig. S3**). Unlike Ulrich *et al.* who assembled complexes from purified RED and SMU1 subdomains produced separately in *E. coli* (29), we chose a co-expression strategy which allowed us to first delineate in HEK-293T cells and then to co-purify from *E. coli* a very stable RED_{mid}-$SMU1_{Nter}$ complex. RED and SMU1 are part of the spliceosomal pre-catalytic B complex, whose molecular architecture was very recently elucidated by cryo-EM (35). Fitting of our atomic structure of RED_{mid}-$SMU1_{Nter}$ enabled us to refine the cryo-EM 3D model by applying the conformational constraint imposed by the newly revealed ß-sheet:ß-sheet interface between RED_{mid} and $SMU1_{Nter}$. The model (**SI Appendix, Fig. S8**) highlights a major structural role for RED, as it is positioned at the interface of the SMU1 LisH motif-based dimerization domain and the SF3B1 core spliceosomal factor. This pivotal position could contribute to a stabilization of the B complex structure during the early stages of spliceosome assembly that precede catalytic activation.

Based on our human RED_{mid}-$SMU1_{Nter}$ structure, we designed pilot experiments and *in silico* screening which led to the identification of two inhibitors, LSP641 and LSP61; they disrupt the RED-SMU1 interaction, reduce RED-SMU1 endogenous levels, inhibit IAV NS1 mRNA splicing and decrease the production of infectious IAV particles. These findings add to a growing list of more than 40 protein-protein interactions that have been successfully targeted with small drug-like molecules, at least *in vitro* (36, 37). Several inhibitors have entered clinical trials, including inhibitors of the p53-MDM2 interaction (38) and inhibitors of the interaction between the HIV-1 integrase and its cofactor LEDGF (39). Prospects for

developing inhibitors seem to be higher for protein-protein interactions in which residues critical for the interaction are concentrated in small binding pockets, as is the case for the α-helix:groove interface between RED_{mid} and $SMU1_{Nter}$. In the recent years much progress has also been made to enhance the therapeutic potential of short cell-permeable peptides as an alternative to conventional therapeutic small molecules (40). In principle a peptide corresponding to the short RED[211-222] α-helix could be considered as a potential inhibitor of RED-SMU1 interaction. However the strong hydrophobicity of this α-helix is likely to prevent its solubilisation and to preclude such a strategy from being successful.

The potential toxicity associated with host-directed therapy also needs to be carefully evaluated. Cultured A549 cells treated with RED-SMU1 targeting compounds LSP461 and LSP61 (this study), or treated with RED-SMU1 targeting siRNAs with a depletion efficiency of 90% (23) did not show cell death. Consistently, RED or SMU1 knock-outs in *C. elegans* or *A. thaliana* are viable (25, 27). However, a cytostatic effect of compound LSP61 was observed, as evidenced by bright field imaging showing a lower density of the cell layer in the absence of dead cells, and ATP quantification supporting a slower accumulation of metabolically active cells in culture wells. This observation is in agreement with previous reports showing that RED and SMU1 jointly regulate alternative splicing of a subset of pre-mRNAs involved in development, apoptosis and cell survival (25-27, 41, 42). The transcriptomic profiling of cells treated with compound LSP61 (or depleted for RED-SMU1 as a reference) will provide a means to investigate how LSP61 affects the expression and splicing of cellular genes, and detect potential adverse effects to guide further drug development (43). Beyond their splicing function, RED and SMU1 are associated with the mitotic spindle (44) and chromatin (45), respectively, and are involved in the control of cell division (44, 46). The dual function of RED-SMU1 raises the question whether our observed anti-viral effect of compounds LSP461 and LSP61 could be related not only to inhibition of viral mRNA splicing (as indicated by a reduced NS2 to NS1 mRNA ratio upon treatment) but also cell cycle arrest. Although this possibility cannot be formally excluded, it seems unlikely as IAV infection *per se* has been shown to induce G0/G1 cell cycle arrest through inhibition of the RhoA/pRb signaling

pathway (47) and down-regulation of cyclin D3 levels (48) in cultured cells. Besides, the tissue naturally targeted by IAVs, *i.e.* the airway epithelium, is essentially quiescent in healthy hosts (49). However, mitogenic stimulation through intra-tracheal administration of the keratinocyte growth factor in mice was found to induce the proliferation of alveolar type II cells (normally quiescent by more than 99%), and this increased their susceptibility to IAV infection (50). The authors suggest that the enhanced mortality due to influenza in infants or cigarette smokers could be related to a higher fraction of proliferating alveolar type II cells in these patients. Under this hypothesis, compounds targeting RED-SMU1 might show a double effect of inhibiting IAV replication through splicing modulation, and limiting the intrapulmonary spread of IAV infection through cytostatic activity.

Over the last two decades a growing number of small molecules that inhibit the spliceosome assembly or function have been identified, but many of them have yet to be characterized regarding their target and mechanism of action. The most documented are SF3B1 inhibitors of the spliceostatins, pladienolides and sudemycins families (51-53). Although these drugs target a core splicing factor, there is evidence for a certain degree of selectivity. SF3B1 inhibitors affect splicing of pre-mRNAs associated with cell cycle regulation and apoptosis, and inhibit growth of cultured cancer cell lines at nM concentrations while cells derived from normal tissues are less sensitive (for a review see (54, 55)). Preclinical studies have suggested that splicing modulation by SF3B1 inhibitors can be well tolerated *in vivo* and show potential for the treatment of several types of cancers (56-58). Taking these data into account, together with the absence of observed cytotoxicity of LSP641 and LSP61 in our experiments, and with the fact that a topical and short time course treatment can be considered in the case of acute IAV infections, compounds targeting the RED-SMU1 complex can reasonably be expected to show clinical safety and efficacy in influenza therapy. Our $SMU1_{Nter}$-LSP641 co-structure provides a valuable basis for chemical optimization in order to select compounds with improved activity, specificity and pharmacological properties, which can be tested *in vivo* in preclinical animal models for IAV infection. Such optimized RED-SMU1 disrupting compounds could be active against a wide

range of IAVs, and be less likely to select for resistance mutants. Interestingly, RED and SMU1 were identified as hits in two high-throughput screens looking for cellular factors involved in HIV-1 life cycle (59, 60). SMU1 was also found to be associated to the E6 protein of the high-risk HPV18 human papillomavirus (61). Therefore RED-SMU1 disrupting compounds might not only be active against IAVs but against a wider range of viruses that make use of the RED-SMU1 splicing complex. Besides potential applications as antivirals, our small molecule inhibitors might also serve as tools to dissect the early stages of spliceosome assembly, and lead to potential applications as anti-cancer agents (54, 62, 63).

Materials and Methods

Cells, viruses, plasmids and reagents. See **SI Appendix** for detailed information

In cellulo split luciferase-based interaction assays

The split-luciferase protein complementation assays were performed as described in (64). Briefly, HEK-293T or A549 cells were seeded in 96-well white opaque plates (Greiner Bio-One) and co-transfected with 100 ng of each indicated pGluc1-P1 and pGluc2-P2 plasmids, where P1 and P2 represent proteins or protein subdomains of interest. The polyethylenimine PEI (Polysciences Inc) and JetPRIME (Polyplus Transfection) transfection reagents were used with HEK-293T and A549 cells, respectively. Normalized luciferase values were determined as described in (23, 64). At 24 h post-transfection, the luciferase enzymatic activities were measured using the *Renilla* luciferase assay system (Promega) and a Berthold Centro XS luminometer. When cell-based interaction assays were performed for compound screening, control HEK-293T cells transfected with a full-length Gaussia luciferase expression plasmid were incubated in parallel with tested compounds or DMSO alone. The split-luciferase values were normalized with respect to control full-length luciferase signals.

Protein expression in E. coli and protein purification

The pETM11-SMU1$_{Nter}$ plasmid was transformed in *E. coli* BL21-CodonPlus (Agilent). Cultures were grown at 37°C in LB containing kanamycin (30 µg/mL) and chloramphenicol (34 µg/mL). When the OD_{600nm} reached 0.6-0.8, the cultures were cooled down to 18°C and expression induced with 0.3 mM isopropyl-thiogalactopyranose (IPTG). The cultures were incubated overnight at 18°C before centrifugation. For the SMU1$_{Nter}$-RED$_{mid}$ complex, a co-expression strategy was set up. The pETM11-RED$_{mid}$ plasmid was transformed in *E. coli* BL21-RIL-SMU1$_{Nter}$ competent cells and expression performed using the protocol described above.Cell pellets were resuspended in lysis buffer (50 mM Hepes pH7.5, 150-500 mM

NaCl, 1 mM β-mercaptoethanol (βme)), and sonicated. After centrifugation, the supernatant was complemented with imidazole to reach 25mM and loaded on a nickel affinity column (NiNTA, GIAGEN). The resin was washed with a high salt buffer (50 mM Hepes pH7.5, 1 M NaCl,1 mM βme). The recombinant proteins were eluted with elution buffer (50 mM Hepes pH7.5, 1 M NaCl, 1 mM βme, 300mM imidazole). Protein were dialyzed with TEV protease overnight against the buffer without imidazole, loaded on a second NiNTA column, concentrated and loaded on a size exclusion column, a HiLoad 16/600 Superdex 75 (GE Healthcare) for $SMU1_{Nter}$ or a Superdex 200 Increase 10/300GL (GE Healthcare) for the $SMU1_{Nter}$-RED_{mid} complex. Fractions of interest were concentrated between 5 and 15 mg/mL.

Structure determination

For $SMU1_{Nter}$, the crystals (native and Se-Met derivative) were obtained in 0.1 M Bis-Tris pH5.5, 16-20 % PEG 10K, 0.1 M ammonium acetate and cryoprotected in the same solution + 30 % glycerol. Data were processed with the XDS package (65). For experimental phasing of $SMU1_{Nter}$ a highly redundant single wavelength anomalous dataset of a Se-Methionine (Se-Met) derived crystal was collected to 2.1 Å resolution at the peak of the Se-Met signal, as measured by X-ray fluorescence, on ID29 (66) at the European Synchrotron Radiation Facility (ESRF). For structural solution 8 Se-Met sites were located on the basis of their anomalous differences using SHELXC/D/E (67). These sites were subsequently refined and experimental phases were calculated using the single anomalous dispersion (SAD) procedure in SHARP (68). These phases were further improved by density modification followed by model building with the Buccaneer software (69). Model building and refinement were performed using CCP4i suite program for crystallography (PHASER, ARP/wARP, REFMAC5, COOT) (70-74).

For the RED_{mid}-$SMU1_{Nter}$ complex, the crystals (native and Se-Met derivative) were obtained in 0.1 M Hepes pH 7.0-7.5, 8-10 % PEG 8K and cryoprotected in the same solution + 30 % glycerol. Data were processed with XDS and the structure was solved by molecular replacement using the native $SMU1_{Nter}$ structure. The model was built using the anomalous

signal of a Se-met derivative dataset for an accurate side chains attribution, and the final refinement was performed using the software mentioned above.

For the $SMU1_{Nter}$ + LSP641 complex, a mother solution of LSP641 was prepared at 125 mM in DMSO. The co-crystals of $SMU1_{Nter}$ (10 mg/mL) + 2.5 mM LSP641 were obtained in 0.1 M Bis-Tris pH 6, 16-20 % PEG 10K, 0.2 M ammonium acetate and cryoprotected in the same solution + 30 % glycerol. Data collection, processing and model building were performed as described above.

In silico screening

Docking experiments were performed using the LibDock protocol, as implemented in Discovery Studio (Discovery Studio Modeling Environment, release 4.5; Dassault Systemes BIOVIA: San Diego, 2015), an interface to the LibDock program developed by Diller and Merz (75). LibDock uses protein site features referred to as HotSpots that fall into two categories: polar and apolar HotSpots. The receptor HotSpot file was calculated prior to the docking procedure. Random ligand conformations were generated from the initial ligand structure through high-temperature molecular dynamics using the BEST algorithm before docking. The rigid ligand poses were placed into the active site and HotSpots were matched as triplets. The poses were pruned and a final optimization step was performed before the poses were scored. Ligand hydrogens, which were removed during the docking process, were added back to the ligand poses and optimized by minimization. The poses with the highest LibDock scores were retained and clustered according to their binding mode.

RNA extraction and reverse transcription-quantitative PCR

Total RNA and poly(A)+ RNAs were extracted subsequently using the RNeasy Mini Kit (Qiagen) and Oligotex mRNA Mini kit (Qiagen) following the manufacturer's protocol. Reverse transcription (RT) was performed on 5-10 ng of total mRNA (or poly(A)+ RNA equivalent) using the Maxima First Strand cDNA Synthesis Kit (Thermo Scientific). Quantitative real-time PCR was performed on 2 µL of a 1/10 dilution of the RT reaction using

the Luminaris Color Probe qPCR Master Mix (Thermo Scientific) and a Light Cycler 480 (Roche). The levels of NS1/NS2 and M1/M2 mRNAs were determined and normalized with respect to GAPDH mRNA levels using the protocol described in (23). The levels of PB2/PB2-S1 mRNAs were determined by semi-quantitative RT-PCR as described in (34).

Data Availability Statement

Structure coordinates and diffraction data are available on the Protein Data Bank (http://www.pdb.org) under accession codes PDB: 6Q8F ($SMU1_{Nter}$), 6Q8I (RED_{mid}-$SMU1_{Nter}$), and 6Q8J ($SMU1_{Nter}$-LSP641).

Acknowledgments

We thank Sylvie van der Werf and Stephen Cusack for their support, Rodolphe Alves de Sousa for access to the database for virtual screening and to the Paris-Descartes 2MI platform facilities, Jean-Marie Bourhis, Wim Burmeister, Mariette Matondo, Thibaut Chaze and Christiane Branlant for their help and/or discussions, and the staff of the ESRF-EMBL Joint Structural Biology Group for access to ESRF beamlines. UA is part of the Pasteur-Paris University (PPU) International PhD Program, which has received funding from the European Union's Horizon 2020 research and innovation programme under the Marie Sklodowska-Curie grant agreement No 665807, and from the Institut Carnot Pasteur Microbes & Santé. LT, TC and RR were funded through the ANR RNAP-IAV (ANR-14-CE09-0017). GF received funding from the Institut Carnot Pasteur Microbes & Santé. This study was supported by the European Commission FP7 project FLUPHARM (Grant Agreement No 259751). The authors acknowledge access to the CNRS French National Chemical Library, to the 2MI modeling platform (UMR 8601 CNRS, Université Paris Descartes) and to the biophysical platforms of the Grenoble Instruct-ERIC Center (ISBG; UMS 3518 CNRS-CEA-UGA-EMBL) with support from FRISBI (ANR-10-INSB-05-02) and GRAL (ANR-10-LABX-49-01), within the Grenoble Partnership for Structural Biology (PSB).

References

1. Kaufmann SHE, Dorhoi A, Hotchkiss RS, & Bartenschlager R (2018) Host-directed therapies for bacterial and viral infections. *Nat Rev Drug Discov* 17(1):35-56.

2. Zumla A*, et al.* (2016) Host-directed therapies for infectious diseases: current status, recent progress, and future prospects. *Lancet Infect Dis* 16(4):e47-63.

3. Krammer F*, et al.* (2018) Influenza. *Nat Rev Dis Primers* 4(1):3.

4. Hurt AC (2014) The epidemiology and spread of drug resistant human influenza viruses. *Curr Opin Virol* 8:22-29.

5. Lackenby A*, et al.* (2018) Global update on the susceptibility of human influenza viruses to neuraminidase inhibitors and status of novel antivirals, 2016-2017. *Antiviral Res* 157:38-46.

6. Hurt AC*, et al.* (2012) Characteristics of a widespread community cluster of H275Y oseltamivir-resistant A(H1N1)pdm09 influenza in Australia. *J Infect Dis* 206(2):148-157.

7. Takashita E*, et al.* (2015) Characterization of a large cluster of influenza A(H1N1)pdm09 viruses cross-resistant to oseltamivir and peramivir during the 2013-2014 influenza season in Japan. *Antimicrob Agents Chemother* 59(5):2607-2617.

8. Meijer A*, et al.* (2009) Oseltamivir-resistant influenza virus A (H1N1), Europe, 2007-08 season. *Emerg Infect Dis* 15(4):552-560.

9. Bank C*, et al.* (2016) An experimental evaluation of drug-induced mutational meltdown as an antiviral treatment strategy. *Evolution* 70(11):2470-2484.

10. Goldhill DH*, et al.* (2018) The mechanism of resistance to favipiravir in influenza. *Proc Natl Acad Sci U S A* 115(45):11613-11618.

11. Hayden FG*, et al.* (2018) Baloxavir Marboxil for Uncomplicated Influenza in Adults and Adolescents. *N Engl J Med* 379(10):913-923.

12. Koszalka P, Tilmanis D, & Hurt AC (2017) Influenza antivirals currently in late-phase clinical trial. *Influenza Other Respir Viruses* 11(3):240-246.

13. McKimm-Breschkin JL*, et al.* (2018) Prevention and treatment of respiratory viral infections: Presentations on antivirals, traditional therapies and host-directed interventions at the 5th ISIRV Antiviral Group conference. *Antiviral Res* 149:118-142.

14. Ramos EL*, et al.* (2015) Efficacy and safety of treatment with an anti-m2e monoclonal antibody in experimental human influenza. *J Infect Dis* 211(7):1038-1044.

15. Wollacott AM*, et al.* (2016) Safety and Upper Respiratory Pharmacokinetics of the Hemagglutinin Stalk-Binding Antibody VIS410 Support Treatment and Prophylaxis Based on Population Modeling of Seasonal Influenza A Outbreaks. *EBioMedicine* 5:147-155.

16. Byrn RA*, et al.* (2015) Preclinical activity of VX-787, a first-in-class, orally bioavailable inhibitor of the influenza virus polymerase PB2 subunit. *Antimicrob Agents Chemother* 59(3):1569-1582.

17. Rossignol JF (2014) Nitazoxanide: a first-in-class broad-spectrum antiviral agent. *Antiviral Res* 110:94-103.

18. Haffizulla J*, et al.* (2014) Effect of nitazoxanide in adults and adolescents with acute uncomplicated influenza: a double-blind, randomised, placebo-controlled, phase 2b/3 trial. *Lancet Infect Dis* 14(7):609-618.

19. Colombo RE*, et al.* (2016) A phase 1 randomized, double-blind, placebo-controlled, crossover trial of DAS181 (Fludase(R)) in adult subjects with well-controlled asthma. *BMC Infect Dis* 16:54.

20. Zenilman JM*, et al.* (2015) Phase 1 clinical trials of DAS181, an inhaled sialidase, in healthy adults. *Antiviral Res* 123:114-119.

21. van de Wakker SI, Fischer MJE, & Oosting RS (2017) New drug-strategies to tackle viral-host interactions for the treatment of influenza virus infections. *Eur J Pharmacol* 809:178-190.

22. Watanabe T & Kawaoka Y (2015) Influenza virus-host interactomes as a basis for antiviral drug development. *Curr Opin Virol* 14:71-78.

23. Fournier G*, et al.* (2014) Recruitment of RED-SMU1 complex by Influenza A Virus RNA polymerase to control Viral mRNA splicing. *PLoS Pathog* 10(6):e1004164.

24. Bessonov S, Anokhina M, Will CL, Urlaub H, & Luhrmann R (2008) Isolation of an active step I spliceosome and composition of its RNP core. *Nature* 452(7189):846-850.

25. Chung T, Wang D, Kim CS, Yadegari R, & Larkins BA (2009) Plant SMU-1 and SMU-2 homologues regulate pre-mRNA splicing and multiple aspects of development. *Plant Physiol* 151(3):1498-1512.

26. Papasaikas P, Tejedor JR, Vigevani L, & Valcarcel J (2015) Functional splicing network reveals extensive regulatory potential of the core spliceosomal machinery. *Mol Cell* 57(1):7-22.

27. Spartz AK, Herman RK, & Shaw JE (2004) SMU-2 and SMU-1, Caenorhabditis elegans homologs of mammalian spliceosome-associated proteins RED and fSAP57, work together to affect splice site choice. *Mol Cell Biol* 24(15):6811-6823.

28. Hegele A*, et al.* (2012) Dynamic protein-protein interaction wiring of the human spliceosome. *Mol Cell* 45(4):567-580.

29. Ulrich AKC, Schulz JF, Kamprad A, Schutze T, & Wahl MC (2016) Structural Basis for the Functional Coupling of the Alternative Splicing Factors Smu1 and RED. *Structure* 24(5):762-773.

30. Boxem M*, et al.* (2008) A protein domain-based interactome network for C. elegans early embryogenesis. *Cell* 134(3):534-545.

31. Le Corre L*, et al.* (2010) Synthesis and biological evaluation of a triazole-based library of pyrido[2,3-d]pyrimidines as FGFR3 tyrosine kinase inhibitors. *Org Biomol Chem* 8(9):2164-2173.

32. Matrosovich M, Matrosovich T, Carr J, Roberts NA, & Klenk HD (2003) Overexpression of the alpha-2,6-sialyltransferase in MDCK cells increases influenza virus sensitivity to neuraminidase inhibitors. *J Virol* 77(15):8418-8425.

33. Seitz C, Frensing T, Hoper D, Kochs G, & Reichl U (2010) High yields of influenza A virus in Madin-Darby canine kidney cells are promoted by an insufficient interferon-induced antiviral state. *J Gen Virol* 91(Pt 7):1754-1763.

34. Yamayoshi S, Watanabe M, Goto H, & Kawaoka Y (2016) Identification of a Novel Viral Protein Expressed from the PB2 Segment of Influenza A Virus. *J Virol* 90(1):444-456.

35. Bertram K*, et al.* (2017) Cryo-EM Structure of a Pre-catalytic Human Spliceosome Primed for Activation. *Cell* 170(4):701-713 e711.

36. Arkin MR, Tang Y, & Wells JA (2014) Small-molecule inhibitors of protein-protein interactions: progressing toward the reality. *Chem Biol* 21(9):1102-1114.

37. Scott DE, Bayly AR, Abell C, & Skidmore J (2016) Small molecules, big targets: drug discovery faces the protein-protein interaction challenge. *Nat Rev Drug Discov* 15(8):533-550.

38. Zhang B, Golding BT, & Hardcastle IR (2015) Small-molecule MDM2-p53 inhibitors: recent advances. *Future Med Chem* 7(5):631-645.

39. Weydert C, De Rijck J, Christ F, & Debyser Z (2016) Targeting Virus-host Interactions of HIV Replication. *Curr Top Med Chem* 16(10):1167-1190.

40. Fosgerau K & Hoffmann T (2015) Peptide therapeutics: current status and future directions. *Drug Discov Today* 20(1):122-128.

41. Dassah M, Patzek S, Hunt VM, Medina PE, & Zahler AM (2009) A genetic screen for suppressors of a mutated 5' splice site identifies factors associated with later steps of spliceosome assembly. *Genetics* 182(3):725-734.

42. Kanno T*, et al.* (2017) A Genetic Screen for Pre-mRNA Splicing Mutants of Arabidopsis thaliana Identifies Putative U1 snRNP Components RBM25 and PRP39a. *Genetics* 207(4):1347-1359.

43. Verbist B*, et al.* (2015) Using transcriptomics to guide lead optimization in drug discovery projects: Lessons learned from the QSTAR project. *Drug Discov Today* 20(5):505-513.

44. Yeh PC, Yeh CC, Chen YC, & Juang YL (2012) RED, a spindle pole-associated protein, is required for kinetochore localization of MAD1, mitotic progression, and activation of the spindle assembly checkpoint. *The Journal of biological chemistry* 287(15):11704-11716.

45. Ren L*, et al.* (2013) Loss of Smu1 function de-represses DNA replication and over-activates ATR-dependent replication checkpoint. *Biochem Biophys Res Commun* 436(2):192-198.

46. Shah VJ & Maddika S (2018) CRL7(SMU1) E3 ligase complex-driven H2B ubiquitylation functions in sister chromatid cohesion by regulating SMC1 expression. *J Cell Sci* 131(8).

47. Jiang W*, et al.* (2013) Influenza A virus NS1 induces G0/G1 cell cycle arrest by inhibiting the expression and activity of RhoA protein. *J Virol* 87(6):3039-3052.

48. Fan Y*, et al.* (2017) Cell Cycle-independent Role of Cyclin D3 in Host Restriction of Influenza Virus Infection. *J Biol Chem* 292(12):5070-5088.

49. Teixeira VH*, et al.* (2013) Stochastic homeostasis in human airway epithelium is achieved by neutral competition of basal cell progenitors. *Elife* 2:e00966.

50. Nikolaidis NM*, et al.* (2017) Mitogenic stimulation accelerates influenza-induced mortality by increasing susceptibility of alveolar type II cells to infection. *Proc Natl Acad Sci U S A* 114(32):E6613-E6622.

51. Kaida D*, et al.* (2007) Spliceostatin A targets SF3b and inhibits both splicing and nuclear retention of pre-mRNA. *Nat Chem Biol* 3(9):576-583.

52. Kotake Y*, et al.* (2007) Splicing factor SF3b as a target of the antitumor natural product pladienolide. *Nat Chem Biol* 3(9):570-575.

53. Fan L, Lagisetti C, Edwards CC, Webb TR, & Potter PM (2011) Sudemycins, novel small molecule analogues of FR901464, induce alternative gene splicing. *ACS Chem Biol* 6(6):582-589.

54. Bonnal S, Vigevani L, & Valcarcel J (2012) The spliceosome as a target of novel antitumour drugs. *Nat Rev Drug Discov* 11(11):847-859.

55. Effenberger KA, Urabe VK, & Jurica MS (2017) Modulating splicing with small molecular inhibitors of the spliceosome. *Wiley Interdiscip Rev RNA* 8(2).

56. Hsu TY*, et al.* (2015) The spliceosome is a therapeutic vulnerability in MYC-driven cancer. *Nature* 525(7569):384-388.

57. Lagisetti C*, et al.* (2009) Synthetic mRNA splicing modulator compounds with in vivo antitumor activity. *J Med Chem* 52(22):6979-6990.

58. Lee SC*, et al.* (2016) Modulation of splicing catalysis for therapeutic targeting of leukemia with mutations in genes encoding spliceosomal proteins. *Nat Med* 22(6):672-678.

59. Jager S*, et al.* (2012) Global landscape of HIV-human protein complexes. *Nature* 481(7381):365-370.

60. Konig R*, et al.* (2008) Global analysis of host-pathogen interactions that regulate early-stage HIV-1 replication. *Cell* 135(1):49-60.

61. Rozenblatt-Rosen O*, et al.* (2012) Interpreting cancer genomes using systematic host network perturbations by tumour virus proteins. *Nature* 487(7408):491-495.

62. Lee SC & Abdel-Wahab O (2016) Therapeutic targeting of splicing in cancer. *Nat Med* 22(9):976-986.

63. Salton M & Misteli T (2016) Small Molecule Modulators of Pre-mRNA Splicing in Cancer Therapy. *Trends Mol Med* 22(1):28-37.

64. Cassonnet P*, et al.* (2011) Benchmarking a luciferase complementation assay for detecting protein complexes. *Nat Methods* 8(12):990-992.

65. Kabsch W (2010) Integration, scaling, space-group assignment and post-refinement. *Acta Crystallogr D Biol Crystallogr* 66(Pt 2):133-144.

66. de Sanctis D*, et al.* (2012) ID29: a high-intensity highly automated ESRF beamline for macromolecular crystallography experiments exploiting anomalous scattering. *J Synchrotron Radiat* 19(Pt 3):455-461.

67. Sheldrick GM (2010) Experimental phasing with SHELXC/D/E: combining chain tracing with density modification. *Acta Crystallogr D Biol Crystallogr* 66(Pt 4):479-485.

68. de La Fortelle E & Bricogne G (1997) [27] Maximum-likelihood heavy-atom parameter refinement for multiple isomorphous replacement and multiwavelength anomalous diffraction methods. *Methods Enzymol* 276:472-494.

69. Cowtan K (2006) The Buccaneer software for automated model building. 1. Tracing protein chains. *Acta Crystallogr D Biol Crystallogr* 62(Pt 9):1002-1011.

70. Cohen SX*, et al.* (2008) ARP/wARP and molecular replacement: the next generation. *Acta Crystallogr D Biol Crystallogr* 64(Pt 1):49-60.

71. Emsley P & Cowtan K (2004) Coot: model-building tools for molecular graphics. *Acta Crystallogr D Biol Crystallogr* 60(Pt 12 Pt 1):2126-2132.

72. McCoy AJ*, et al.* (2007) Phaser crystallographic software. *J Appl Crystallogr* 40(Pt 4):658-674.

73. Murshudov GN, Vagin AA, & Dodson EJ (1997) Refinement of macromolecular structures by the maximum-likelihood method. *Acta Crystallogr D Biol Crystallogr* 53(Pt 3):240-255.

74. Winn MD*, et al.* (2011) Overview of the CCP4 suite and current developments. *Acta Crystallogr D Biol Crystallogr* 67(Pt 4):235-242.

75. Diller DJ & Merz KM, Jr. (2001) High throughput docking for library design and library prioritization. *Proteins* 43(2):113-124.

76. The PyMOL Molecular Graphics System Version 2.0 Schrödinger LLC.

Figure legends

Figure 1. RED-SMU1 interaction mapping using a cell-based assay.

The *Gaussia princeps* luciferase-based complementation assay was performed as described in the Methods section. Gluc2-fused RED full-length (RED) or indicated subdomains were coexpressed with Gluc1-fused SMU1 full-length (SMU1) or SMU1[1-196] ($SMU1_{Nter}$) by transient transfection in HEK-293T cells. **A.** The normalized luciferase activities are expressed as percentages relative to the activity measured with full-length RED and SMU1 proteins. The data shown are the mean +/- SD of three independent experiments in triplicates. Black and grey bars represent luciferase activities measured in the presence of SMU1 and $SMU1_{Nter}$, respectively. ** : $p<0.01$ (parametric unpaired t-test). On the schematic diagram of RED its characteristic stretch of repeated arginine, glutamic acid and aspartic acid residues is represented by a hatched box. The dotted line highlights the interaction between the two components of the minimal $SMU1_{Nter}$-RED_{mid} complex. **B.** Cell lysates used to determine luciferase activities in A were subsequently analysed by western blot using antibodies specific for *Gaussia princeps* luciferase (Gluc, upper panel) and Glyceraldehyde phosphate deshydrogenase (GAPDH, lower panel). White arrowhead: Gluc1-SMU1; Open arrowhead: Gluc2-RED; Black arrowhead: Gluc2-RED[206-260], renamed Glu2-RED_{mid} in the text.

Figure 2: Crystal structure of the recombinant human RED_{mid}-$SMU1_{Nter}$ complex.

A. Global view of the complex. The RED_{mid} and $SMU1_{Nter}$ proteins are coloured in red and yellow respectively. One monomer of $SMU1_{Nter}$ is shown as a ribbon diagram and the second as a surface representation. **B.** Close-up view of the mixed ß-sheet formed by the interaction of RED[235-257] with the N-terminal ß-strand of a $SMU1_{Nter}$ monomer, and stabilized by the C-terminal surface of the other dimer partner $SMU1_{Nter}$ molecule. **C.** Details of the second interface corresponding to the α-helical part of RED_{mid} inserted into a hydrophobic groove at the surface of $SMU1_{Nter}$. The images were generated using PyMOL (76).

Figure 3. Structure-based analysis of the RED-SMU1 interface.

A. Schematic representation of Interface II. On the helical weel representation of RED (residues 213 to 222), aliphatic residues (in a grey frame) are concentrated at the RED-SMU1 interface. The polar residues (in blue) are exclusively located on the opposite side. **B.** Location of SMU1 and RED residues (coloured in green and purple, respectively) involved in interactions at interface II and subjected to mutagenesis experiments shown in panels C to H. **C-E.** Luciferase-based complementation assays were performed as described in the Methods section with the indicated combinations of wild-type (wt) or mutant proteins. The normalized luciferase activities are expressed as percentages relative to the activity measured in the presence of the wt SMU1 and RED proteins. The data shown are the mean +/- SD of three independent experiments in triplicates, except when SMU1-D57A-E89A was tested in (C): two independent experiments. ** $p<0.01$, *** $p<0.001$ unpaired t-test. **F.** The indicated combinations of wt or mutant SMU1 and RED proteins, fused to the Strep-tag, were transiently co-expressed in HEK-293T cells. Cell lysates were analysed by western blot, using HRP-conjugated Streptactin (lower panel). GAPDH (upper panel) was used as a loading control. **G-H.** Cell lysates used to determine luciferase activities in C and D were subsequently analysed by western blot, using antibodies specific for Gluc (lower panel) and an anti-GAPDH antibody (upper panel).

Figure 4. SMU1$_{Nter}$ binding to compounds LSP641 and LSP61.

A. Flow chart of *in silico* screening and compound evaluation. The indicated assays were performed as described in the Methods section, in the presence of compounds at 60 µM or DMSO. The Venn diagrams show the number of selected compounds. The cut-off applied are indicated in italics (cell viability assay: < 2-fold reduction in CellTiter-Glo signal after 36h incubation with the compound compared to DMSO; RED-SMU1 and IAV replication assays: ≥ 20% and ≥ 80% reduction in Gaussia luciferase and Nanoluc signal, respectively, in the presence of the compound compared to DMSO). **B.** SMU1$_{Nter}$ residues required for efficient binding to RED (coloured in green) and used for filtering of the docking poses. **C.** Chemical

structures of compounds LSP641 and LSP61. **D.** Co-crystal structure of LSP641 in complex with $SMU1_{Nter}$. The LSP641 binding pocket is coloured according to hydrophobicity (blue: hydrophilic, red: hydrophobic). **E.** Residues of SMU1 involved in LSP641 binding. Green: key residues for RED binding which also interact with LSP641. Orange: other residues which strongly interact with LSP641 in the co-crystal structure. **F.** Representative pose of LSP61 upon *in silico* docking on SMU_{Nter}. The LSP61 binding pocket is coloured according to hydrophobicity (blue: hydrophilic, red: hydrophobic). **G.** Residues of SMU1 predictively involved in LSP61 binding. Green: key residues for RED binding which also interact with LSP61 upon molecular docking. Orange: other residues which strongly interact with LSP61 upon molecular docking.

Figure 5. Evaluation of compound LSP61 for RED-SMU1 destabilisation.

A. RED-SMU1 interaction assay. The split-luciferase assay was performed as described in the Methods section. At 8 hours post-transfection (hpt), the A549 cells were incubated with the relevant compounds at the concentrations indicated. The normalized luciferase units measured at 24 hpt are expressed as percentages relative to the DMSO-treated control. The data shown are the mean +/- SD of three independent experiments in triplicates. ** $p<0.005$ (parametric unpaired t-test). **B.** The split luciferase interaction assay was performed as in A, using Gluc1-FOS and Gluc2-JUN plasmids. The data shown are the mean +/- SD of two independent experiments in triplicates. **C.** Effect on the steady-state levels of the endogenous RED and SMU1 proteins. A549 cells were incubated with the indicated concentrations of LSP61 (+) or with DMSO (-) for 24h. Total cell extracts were analyzed by western blot, using antibodies specific for RED, SMU1 and GAPDH. **D.** Cell viability assay. A549 cells were incubated with the indicated concentrations of LSP61 or with DMSO. ATP levels, which reflect the number of viable cells, were determined using the CellTiter-Glo kit (Promega) at the onset of the experiment (T0), and following 24 or 48 hours of incubation (T24, T48). The data shown are the mean of luciferase units +/- SD of two independent experiments in duplicates.

Figure 6. Evaluation of compound LSP61 for anti-IAV activity.

A. Effect on IAV replication. A549 cells were infected with the WSN-Nanoluc or RSV-Firefly virus (0.001 and 0.01 PFU/cell, respectively) and incubated with LSP641 or LSP61 at the indicated concentrations, or with DMSO. The luciferase units measured at 24 hpi are expressed as percentages relative to DMSO-treated control. The data shown are the mean +/- SD of three (WSN-Nanoluc) or two (RSV-luc) independent experiments in triplicates. **p<0.005, ***p<0.0001 (parametric paired t-test). **B-C.** Effect on the production of infectious particles. MDCK-SIAT (B) or A549 cells (C) were infected with the WSN, H1N1pdm09 or H3N2 viruses as indicated, and incubated with 60 µM of LSP61 or with DMSO. At 24, 48, and 72 hpi, the supernatants were collected and viral titers determined by plaque assay. The data are expressed as mean +/- SD of three independent experiments (except for the 24 hpi time-point in C and D : two independent experiments), each in triplicates that were pooled for titration. * p<0.05, ** p<0.01, *** p<0.001, parametric paired t-test. **D.** Effect on NS1 mRNA splicing. A549 cells were infected with the WSN-wt virus (5 PFU/cell), and incubated with 60 µM of LSP641 or LSP61, or with DMSO. After 6 h incubation, polyA+ RNA were extracted and the levels of NS2 and NS1 mRNAs were analyzed by quantitative real-time PCR and normalized with respect to GAPDH mRNA levels. The NS2/NS1 mRNA ratios shown are the mean +/- SD of three independent experiments in duplicates. p=0.01, parametric paired t-test.

Figure 1

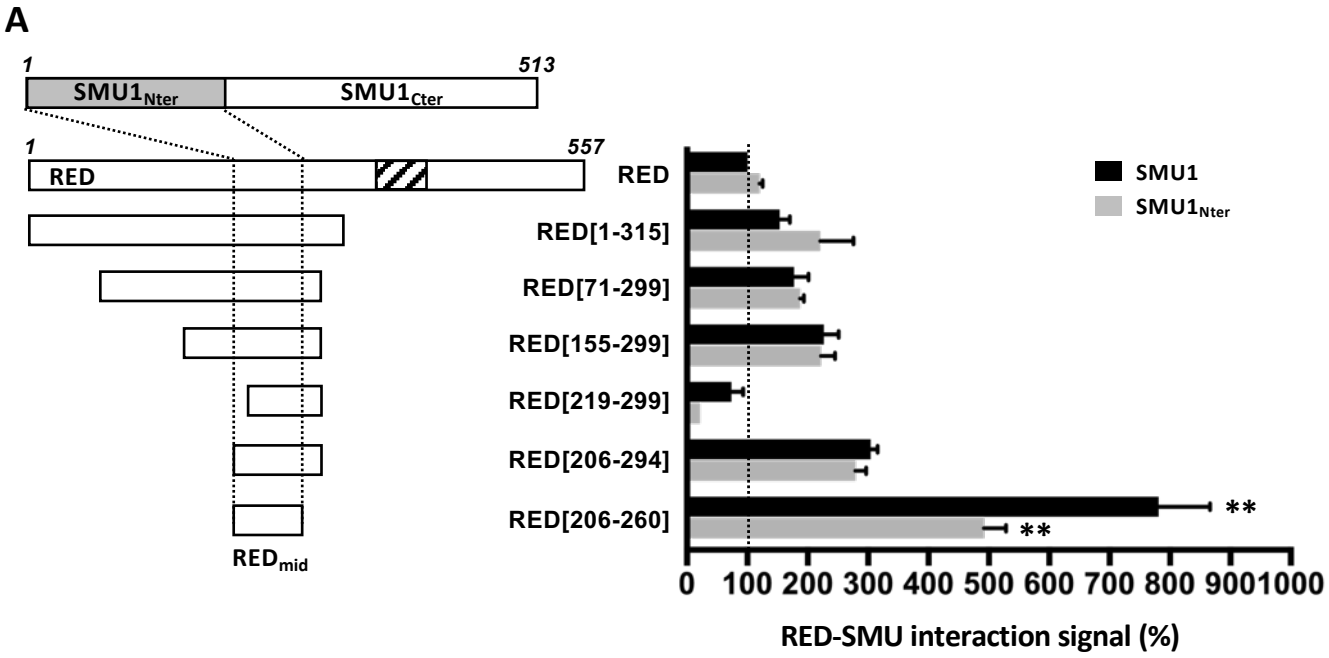
A
1
513
SMU1Nter
SMU1Cter
1
557
RED
REDmid
RED
RED[1-315]
RED[71-299]
RED[155-299]
RED[219-299]
RED[206-294]
RED[206-260]
SMU1
SMU1Nter
**
**
0 100 200 300 400 500 600 700 800 9001000
RED-SMU interaction signal (%)

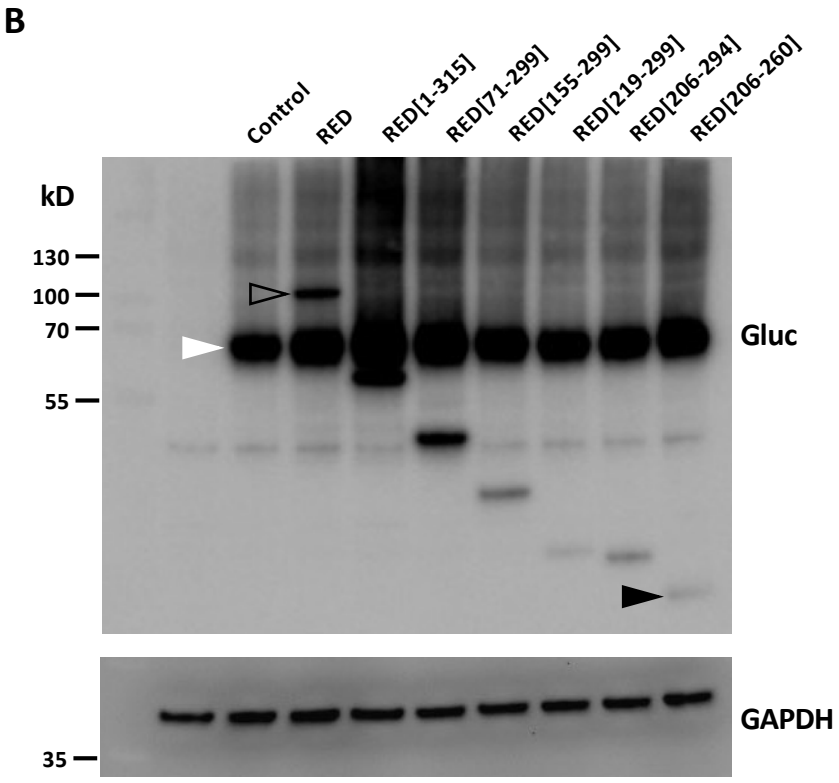
B
Control
RED
RED[1-315]
RED[71-299]
RED[155-299]
RED[219-299]
RED[206-294]
RED[206-260]
kD
130
100
70
55
Gluc
GAPDH
35

Figure 2

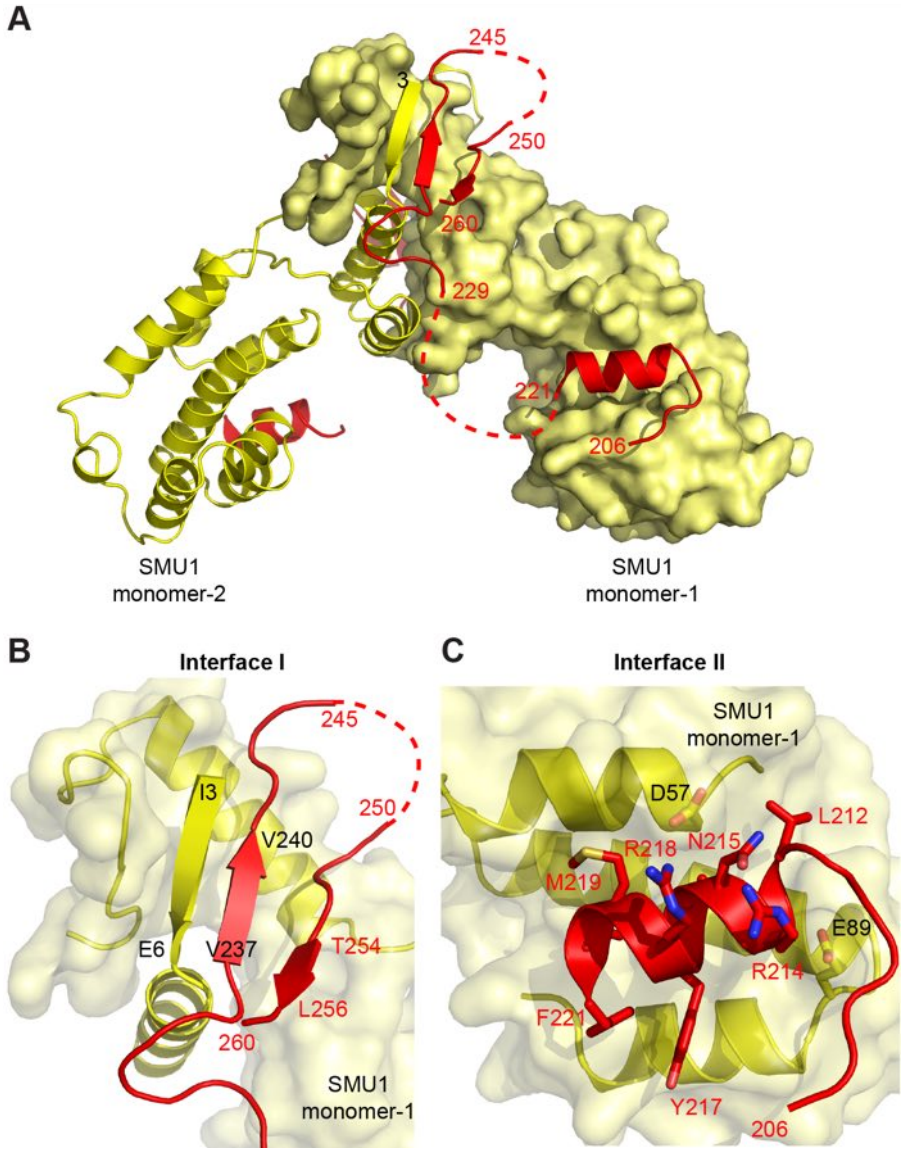
A
245
3
250
260
229
221
206
SMU1
monomer-2
SMU1
monomer-1
B
Interface I
245
I3
250
V240
E6
V237
T254
L256
260
SMU1
monomer-1
C
Interface II
SMU1
monomer-1
D57
L212
R218
N215
M219
E89
R214
F221
Y217
206

Figure 3

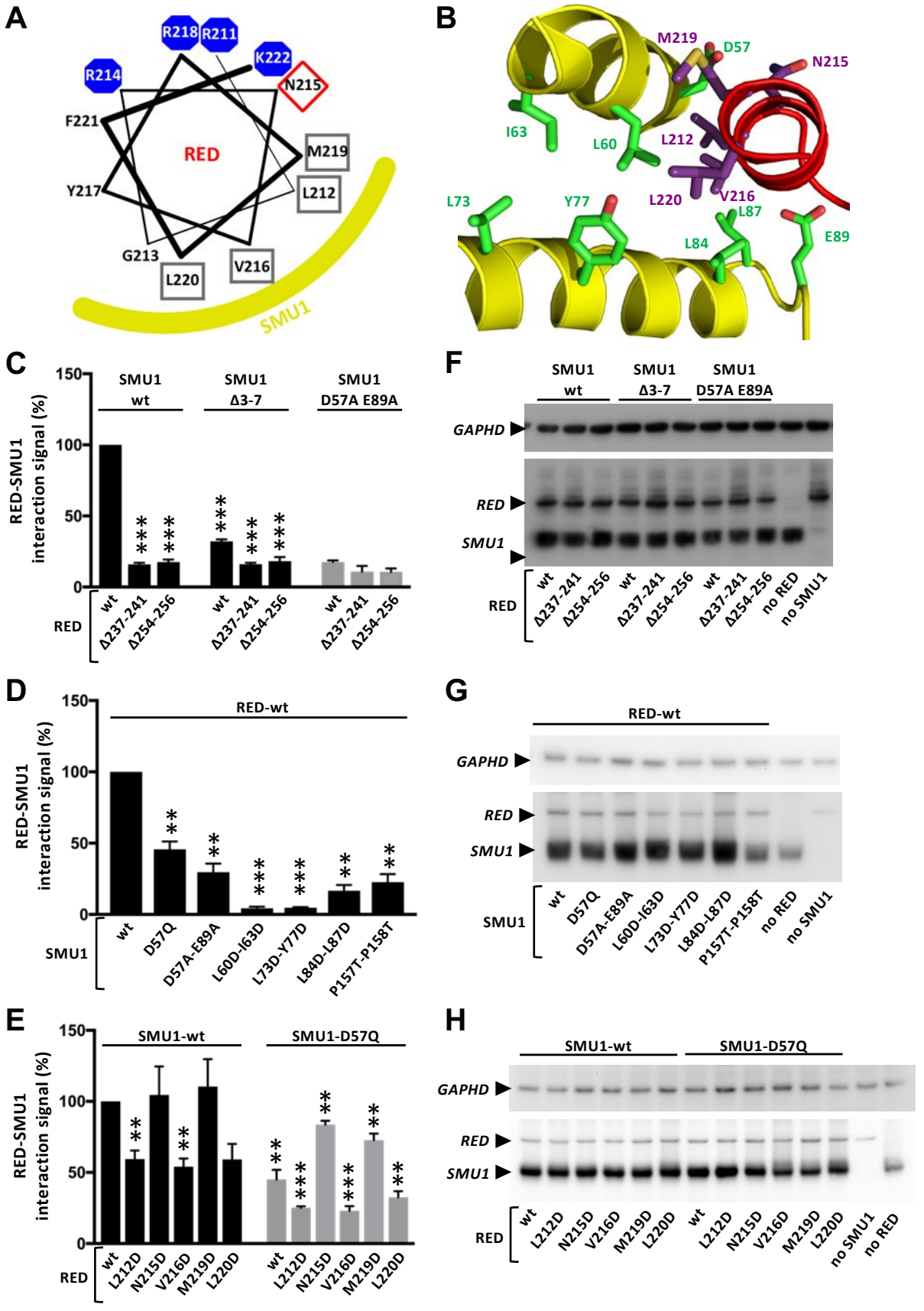
A
R218
R211
K222
R214
N215
F221
RED
M219
Y217
L212
G213
V216
L220
SMU1
B
M219
D57
N215
I63
L60
L212
L73
Y77
L220
V216
L87
L84
E89
C
RED-SMU1 interaction signal (%)
SMU1 wt
SMU1 Δ3-7
SMU1 D57A E89A
RED
wt
Δ237-241
Δ254-256
F
GAPHD
RED
SMU1
no RED
no SMU1
D
RED-wt
SMU1
wt
D57Q
D57A-E89A
L60D-I63D
L73D-Y77D
L84D-L87D
P157T-P158T
G
E
SMU1-wt
SMU1-D57Q
L212D
N215D
V216D
M219D
L220D
H

Figure 4

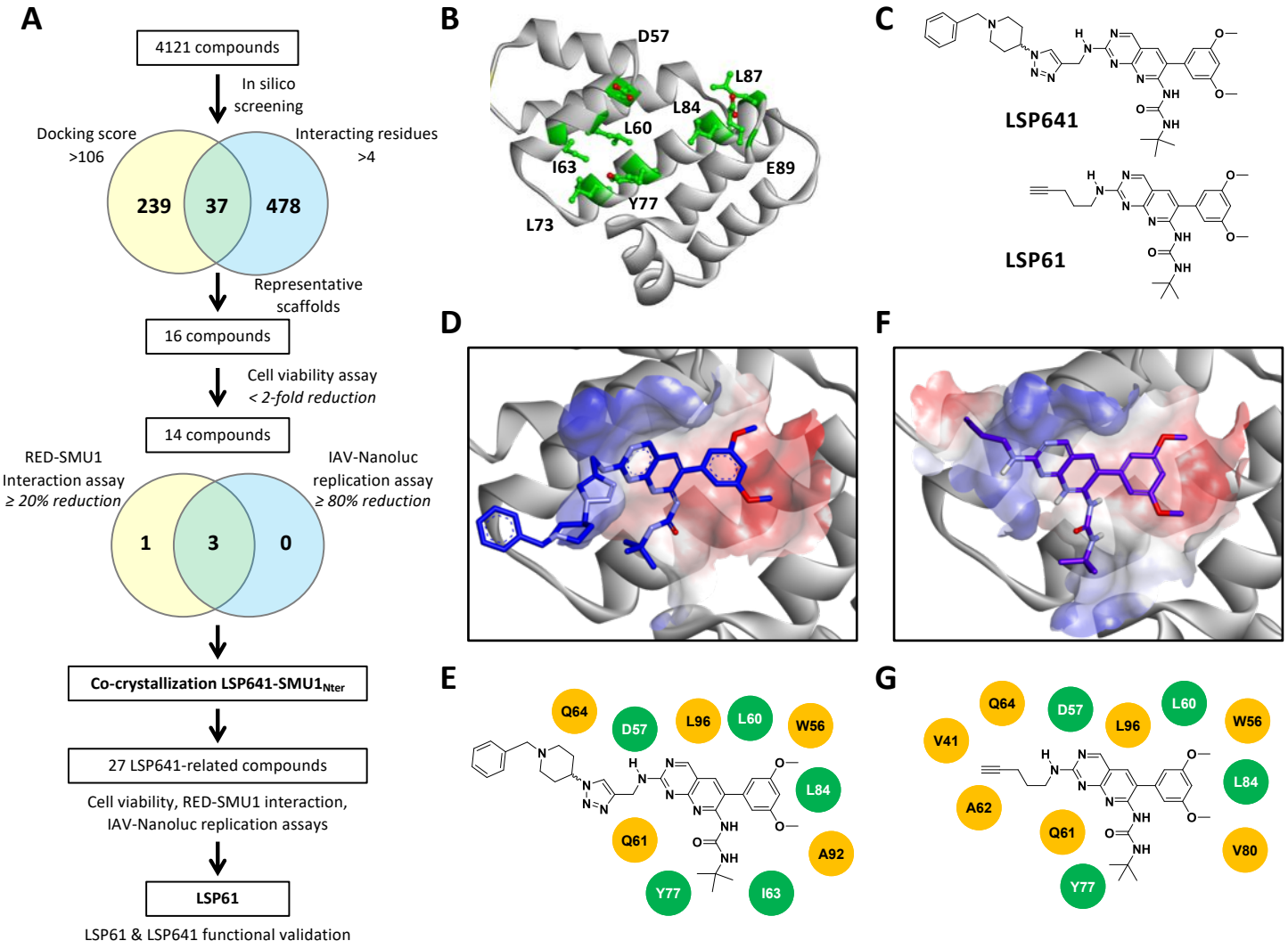
A
4121 compounds
In silico screening
Docking score >106
Interacting residues >4
239
37
478
Representative scaffolds
16 compounds
Cell viability assay
< 2-fold reduction
14 compounds
RED-SMU1 Interaction assay
≥ 20% reduction
IAV-Nanoluc replication assay
≥ 80% reduction
1
3
0
Co-crystallization LSP641-SMU1Nter
27 LSP641-related compounds
Cell viability, RED-SMU1 interaction, IAV-Nanoluc replication assays
LSP61
LSP61 & LSP641 functional validation
B
D57
L87
L84
L60
I63
E89
Y77
L73
C
LSP641
LSP61
D
F
E
Q64
D57
L96
L60
W56
L84
Q61
A92
Y77
I63
G
Q64
D57
L96
L60
W56
V41
L84
A62
Q61
V80
Y77

Figure 5

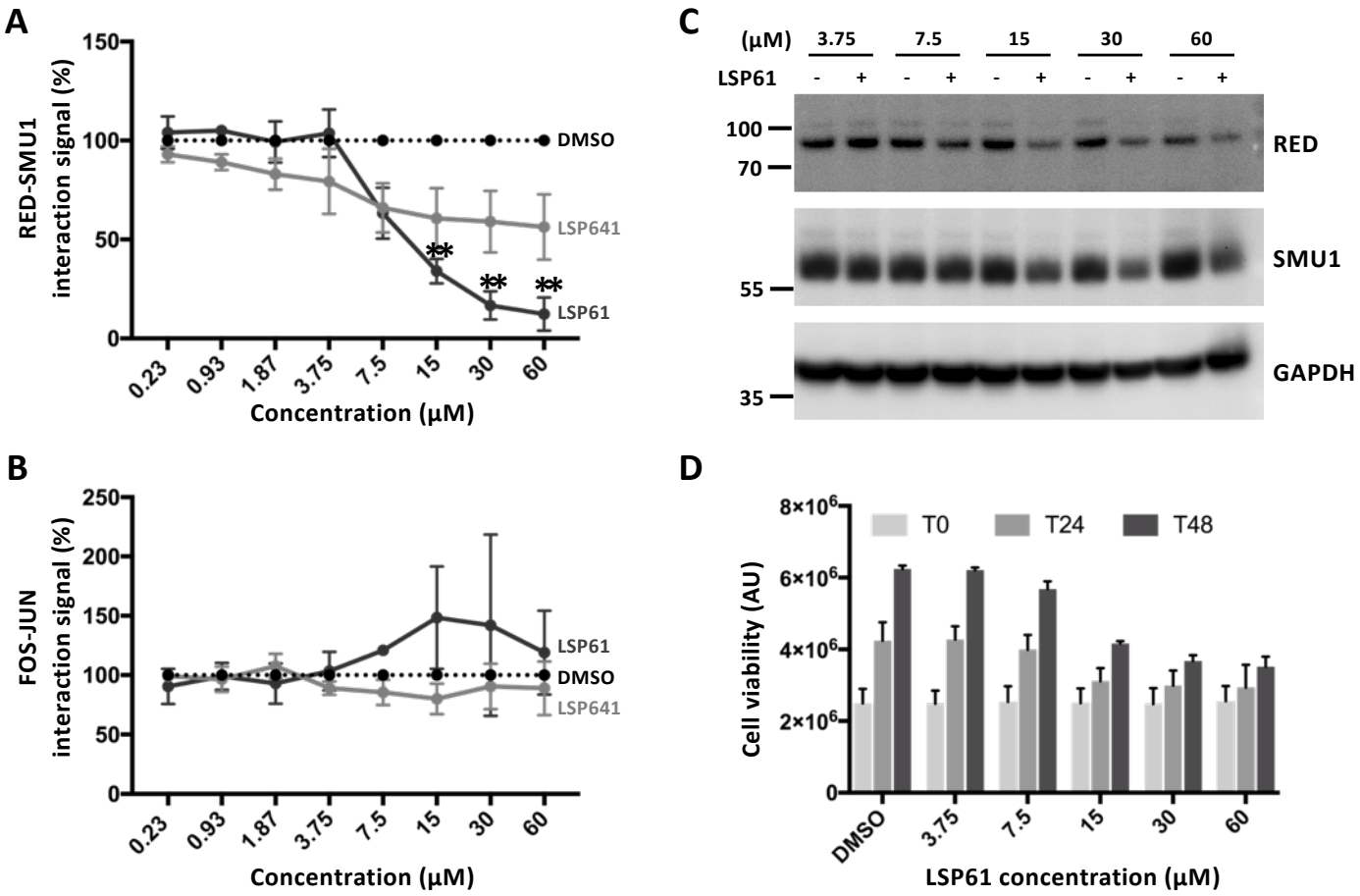
A
RED-SMU1 interaction signal (%)
150
100
50
0
DMSO
LSP641
LSP61
**
**
**
0.23
0.93
1.87
3.75
7.5
15
30
60
Concentration (µM)
C
(µM)
3.75
7.5
15
30
60
LSP61
- + - + - + - + - +
100
70
55
35
RED
SMU1
GAPDH
B
FOS-JUN interaction signal (%)
250
200
150
100
50
0
LSP61
DMSO
LSP641
0.23
0.93
1.87
3.75
7.5
15
30
60
Concentration (µM)
D
Cell viability (AU)
8×10^6
6×10^6
4×10^6
2×10^6
0
T0
T24
T48
DMSO
3.75
7.5
15
30
60
LSP61 concentration (µM)

Figure 6

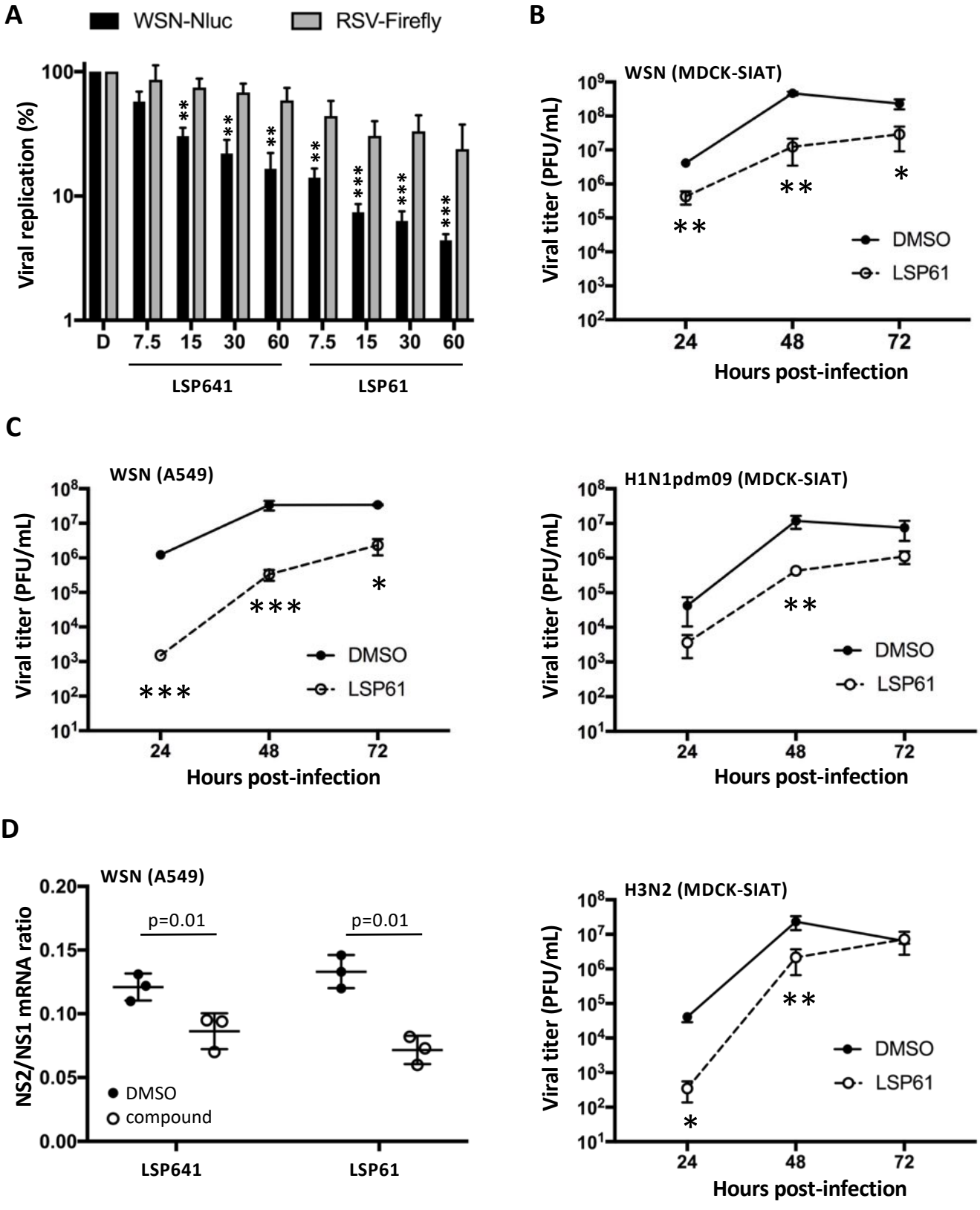
A
WSN-Nluc
RSV-Firefly
Viral replication (%)
100
10
1
D
7.5
15
30
60
7.5
15
30
60
LSP641
LSP61
B
WSN (MDCK-SIAT)
Viral titer (PFU/mL)
DMSO
LSP61
24
48
72
Hours post-infection
C
WSN (A549)
H1N1pdm09 (MDCK-SIAT)
D
WSN (A549)
NS2/NS1 mRNA ratio
p=0.01
p=0.01
DMSO
compound
LSP641
LSP61
H3N2 (MDCK-SIAT)